Journal of Scientific Research & Reports

27(2): 58-71, 2021; Article no.JSRR.67243
ISSN: 2320-0227

Polarization Properties of Solid-Core Photonic Crystal Fibers for 1550 nm

Marco Antonio Cortez-Herrera[1*] and Diana Tentori[1]

[1]Centro de Investigación Científica y de, Educación Superior de Ensenada, Div. Física Aplicada, Carretera Ensenada-Tijuana No. 3918, Zona Playitas, Ensenada, B.C., 22860 México.

Authors' contributions

This work was carried out in collaboration between both authors. Author MACH, designed the experiments, made the acquisition data, performed the statistical analysis and wrote the first draft of the manuscript. Author DT, managed the analysis of data and results, managed the literature searches, managed the structure and ideas of a final version of manuscript. Both authors read and approved the final manuscript.

Article Information

DOI: 10.9734/JSRR/2021/v27i230359
Editor(s):
(1) Dr. Ahmed Mohammed Abu-Dief Mohammed, Sohag University, Egypt.
Reviewers:
(1) Usmeldi, State University of Padang, Indonesia.
(2) Low Khee Lam, RCSI & UCD Malaysia Campus, Malaysia.
Complete Peer review History: http://www.sdiarticle4.com/review-history/67243

Original Research Article

Received 01 February 2021
Accepted 03 April 2021
Published 17 April 2021

ABSTRACT

Due to its microstructure, photonic crystal fibers present wavelength regions with polarization-dependent loss, an aspect not observed in conventional fibers. We include this fact in their polarization characterization. In this research, the use of polarimetric methods to two different types of large-mode-area microstructured fibers has shown that both samples exhibited elliptical birefringence with residual torsion. We present the modifications required to perform the evaluation and justify its theoretical bases.

Keywords: Birefringence; dispersion; photonic crystal fiber.

1. INTRODUCTION

Photonic crystal fibers (PCFs) are a new type of optical fiber. Their characteristics are widely studied because of the new opportunities they offer to optical devices´ design. In particular, due to unwanted symmetry variations introduced during the manufacturing process, photonic

**Corresponding author: E-mail: mcortez@cicese.edu.mx;*

crystal fibers do not maintain the guiding light´s polarization state. The capacity to preserve a specific polarization is a critical characteristic for fiber sensors whose sensitivity to some stimuli is polarization-dependent [1,2]. Polarization performance is also crucial for the development of supercontinuum linearly polarized sources [3], or wavelength tunable sources of circularly-polarized light [4] essential for non-invasive biomedical and imaging applications [5-8].

The methodology used to evaluate the fiber´s birefringence depends on the assumption that absorption for short fiber samples is negligible and it can be uniform (it does not vary randomly). In this case, according to polarization optics, fibers should behave as homogeneous retarders: linear, circular, or elliptical. Even though the general case corresponds to an elliptical retarder, typically, it is assumed the sample presents a linear birefringence. A behavior satisfied by PM or HiBi fibers. Intentional symmetry breaking is introduced to manufacture high-birefringence (HiBi) or polarization-maintaining (PM) fibers whose birefringence exceeds that introduced by external perturbations. These fibers are linearly birefringent.

Thus far, modal birefringence discussion has been based almost entirely on the modal spectrum´s numerical calculations, particularly of the pair of essentially uniformly polarized fundamental modes. The results depend on the specific fiber under investigation [9-16]. Because of the particularity and diversity of fiber structures, it is necessary to develop a measurement procedure to determine its birefringence experimentally.

Procedures used for the evaluation of linear birefringence are in general, more straightforward. Therefore most scientific literature reported for photonic crystal fiber´s polarization evaluation refers to HiBi PCFs [10,13-19]. They are usually characterized by their polarization beat length, measured using a wideband lamp (group birefringence) or monochromatic light source (phase birefringence). Polarization beat length can also be the characterization parameter for a photonic crystal fiber with non-intentionally introduced birefringence [12]. However, to follow the evolution of the state of polarization of the signal as it propagates through the fiber, information on the polarization beat length is not enough. From polarization optics, we know it is necessary to be able to build the fiber birefringence matrix.

Furthermore, since non-intentionally birefringent fibers present a lower-phase birefringence than PM or HiBi fibers, the measurement technique´s accuracy must be higher. This paper offers a precise method allowing the determination of the birefringence matrix of non-intentionally birefringent PCFs presenting elliptical birefringence. The measuring procedure is based on 1) the selection of a wavelength band with uniform transmittance, 2) the use of a fast wavelength scanning technique to identify the type of retarder describing the fiber and 3) the use of the azimuthal scanning of a linearly polarized monochromatic signal to determine the parameters required to build the birefringence matrix [20].

2. THEORY

For fiber lengths shorter than 100 m, single-mode fibers´ birefringence is described using two orthogonal polarization modes whose phase retardation presents a uniform variation [21]. Since the characterization of the ellipticity change of a known state of polarization of light having traveled along the fiber does not supply enough information on the birefringence parameters of the sample [22], several methods based on modulation [23,24,25] and polarimetric techniques [19,26] have been devised.

The model we use for the birefringence evaluation of single-mode photonic crystal fibers assumes that absorption and polarization-dependent loss are negligible. Under this hypothesis, the general model describing the fiber birefringence considers it behaves as an elliptical retarder. Assuming the retarder´s fast birefringence axis is aligned with the reference system, its birefringence is given by equation (1).

$$M_{elip} = \begin{bmatrix} 1 - 2\sin^2(2\mu)\sin^2\left(\frac{\delta_E}{2}\right) & \sin(\delta_E)\sin(2\mu) & \sin^2\left(\frac{\delta_E}{2}\right)\sin(4\mu) \\ -\sin(\delta_E)\sin(2\mu) & \cos(\delta_E) & \sin(\delta_E)\cos(2\mu) \\ \sin^2\left(\frac{\delta_E}{2}\right)\sin(4\mu) & -\sin(\delta_E)\cos(2\mu) & 1 - 2\cos^2(2\mu)\sin^2\left(\frac{\delta_E}{2}\right) \end{bmatrix}, \quad (1)$$

In equation (1) μ is the ellipticity angle of the retarder, being equal to zero for a linear retarder and to π/2 for a circular retarder. Parameter δ_E is the elliptical phase difference, indicating the delay angle between the elliptical polarization eigenmodes. This elliptical phase retardation is related to the linear and circular phase retardations (δ_L and δ_C) by $\delta_E^2 = \delta_L^2 + \delta_c^2$ ($\delta_C = 0$ for a linear retarder and $\delta_L = 0$ for a circular retarder). It is important to remark that the birefringence matrix in equation (1) satisfies Nebraska Convention [27]. Therefore, using classical polarization optics, we can consider the alignment between the fiber birefringence and the state of polarization of light [20]. Furthermore, this Mueller matrix is a unitary rotation operator.

Representing birefringence through a geometric transformation simplifies the understanding of the fiber polarization properties. The intersection of the retarder's axis of rotation with the Poincaré sphere indicates the polarization eigenmodes. Using Mueller matrix formalism, the axis of rotation of a linear retarder lies on the horizontal plane of the Poincaré sphere containing the equator. The intersection of this axis with the equator corresponds to its linear polarization eigenmodes. A circular retarder birefringence is represented by a rotation around the north-south axis of the sphere. This rotation axis crosses the sphere through the north and south poles, corresponding to the right and left polarization eigenmodes. The axis of rotation of an elliptical retarder is inclined (Fig. 1). Therefore, the polarization eigenmodes do not lie on the equator or the poles.

According to the previous model, it is evident that the application of one of these operators (M) to an input state of polarization.

$$S_{out} = M\, S_{in}, \tag{2}$$

Produces an output polarization state whose evolution along the fiber generates a trajectory related to the retarder we are using. As an example, considering a monochromatic linearly polarized input SOP with azimuth angle φ,

$$S_{in}=[\cos(2\varphi) \quad \sin(2\varphi) \quad 0]^t, \tag{3}$$

Where the superindex *t* indicates transpose, and a retarder with an elliptical birefringence [Eq. (1)], we obtain for different azimuth angles of the input linearly polarized signal, dissimilar signal curves, as shown in Fig. 1.

Therefore, the retarder type can be identified following the evolution of a known input SOP as it propagates along the fiber. Although the apparent solution relies on using the cutoff technique, fiber destruction can be avoided by applying wavelength scanning. The method´s ability to follow the phase retardation (δ_E) between the polarization eigenmodes can be understood considering the relation.

$$\delta_E = (2\pi/\lambda)\, \Delta N\, L; \tag{4}$$

Where λ is the signal wavelength, ΔN the fiber birefringence and *L* the fiber length. For the phase retardation δ_E , we obtain a behavior similar to that achieved with the cutoff technique, when the wavelength of a probe signal with a fixed input SOP, launched in a fiber with a fixed length, is scanned.

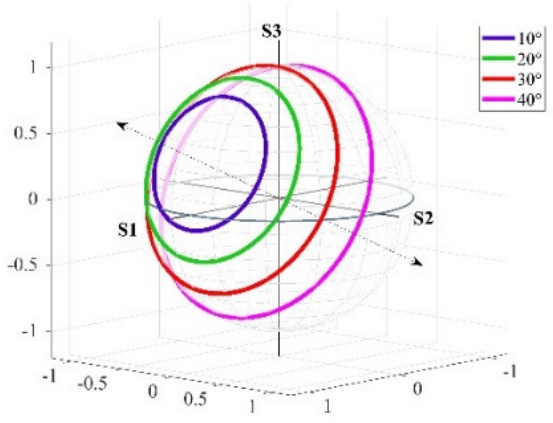

Fig. 1. SOP evolution along a fiber whose birefringence corresponds to an elliptical retarder. Input azimuth angles are 10, 20, 30 and 40 degrees

However, when the azimuth angle of the fast birefringence axis of the retarder forms an angle θ with the measurement reference frame, Eq. (2) should be rewritten as

$$S'_{out}=R(-\theta)MR(\theta)S_{in}, \tag{5}$$

where R(θ) is a rotation matrix represented mathematically as Eq. (6),

$$R(\theta)=\begin{bmatrix}\cos(2\theta) & \sin(2\theta) & 0\\ -\sin(2\theta) & \cos(2\theta) & 0\\ 0 & 0 & 1\end{bmatrix}. \tag{6}$$

Applying equations (1) and (6) in equation (5), we obtained the Stokes vector shown in Eq. (7),

$$S'_{out}=\begin{bmatrix}\sin(2\varphi)\left[\cos^2(2\mu)\sin^2\left(\frac{\delta_E}{2}\right)\sin(4\theta)+\sin(\delta_E)\sin(2\mu)\right]+\cos(2\varphi)\{\cos(\delta_E)\sin^2(2\theta)+\cos^2(2\theta)\zeta\}\\ \cos(2\varphi)\left[\cos^2(2\mu)\sin^2\left(\frac{\delta_E}{2}\right)\sin(4\theta)-\sin(\delta_E)\sin(2\mu)\right]+\sin(2\varphi)\{\cos(\delta_E)\cos^2(2\theta)+\sin^2(2\theta)\zeta\}\\ \cos[2(\varphi-\theta)]\sin^2\left(\frac{\delta_E}{2}\right)\sin(4\mu)-\cos(2\mu)\sin(\delta_E)\sin[2(\varphi-\theta)]\end{bmatrix} \tag{7}$$

Where

$$\zeta=\left[1-2\sin^2\left(\frac{\delta_E}{2}\right)\sin^2(2\mu)\right].$$

Mapping on the Poincaré sphere, the output Stokes parameters measured for the same input linear polarization state (same azimuth angle), we obtain curves to identify the type of retarder associated with the fiber´s birefringence under evaluation. As an example of these results, see figures 6 and 9 in reference [20], showing that both samples present an elliptical birefringence.

There is, however, another possible outcome. The fiber can behave as an elliptical retarder but presenting a residual torsion. In this case, the birefringence matrix is [28,29]

$$M_{r\tau}(\tau,\delta_E,\mu,\theta)=R(-\theta)[R(b\tau)M(\delta_E,\mu)]R(\theta) \tag{8}$$

In this case the polarization evolution curves predicted for different azimuth angles of the input linear polarization present a different behavior. To obtain the results shown in Fig. 2 we used in Eq. (8) the parameters resulting from the numerical simulation presented in [28] (θ= -52°, b = -0.99, τ= -25°, δ_E= -50°, μ = -17°). A similar result was reported in [29, Fig.4(c)] for an erbium-doped fiber whose birefringence was experimentally interrogated using wavelength scanning.

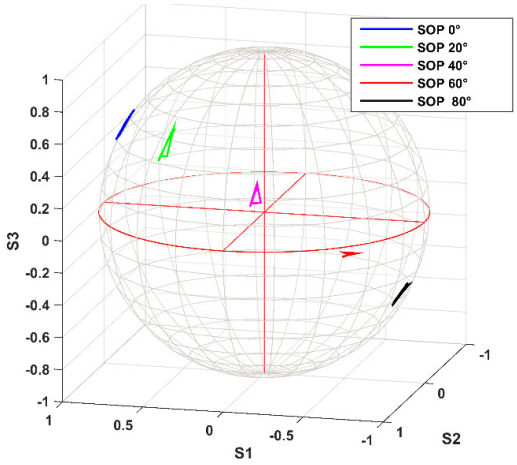

Fig. 2. SOP evolution along a fiber whose birefringence corresponds to an elliptical retarder with residual torsion. Input azimuth angles are shown in the inset

2.1 Experimental Procedure

Due to the step-index between the higher index core and the lower index cladding, light is guided by total internal reflection in conventional optical fibers. On the other hand, in photonic crystal fibers, the guiding mechanism also involves a higher index core and a holey cladding (silica-air microstructure) with a lower average refractive index. Due to this effective step-index between the core and the microstructured cladding, we can consider that total internal reflection is the guiding mechanism, although the cladding microstructure is also involved [30]. Therefore, the sample preparation should avoid processes modifying the fiber microstructure, such as fusion splicing used to couple the photonic crystal fiber to a short length of a single-mode conventional fiber [31,32,33]. The thermal process involved in fusion splicing modify the holey cladding´s original optical properties and might produce an unwanted variation in the transmittance behavior of the fiber induced by these changes. A typical procedure applied to conventional optical fibers consists of installing a connector at the fiber end followed by a polishing treatment. To avoid altering the cladding air holes, we collapsed them only in the vicinity of the fiber´s input and output faces. Then we optically polished the photonic crystal fiber end faces. Finally, we added an FC/UPC connector as described below.

We should also mention that Wegmuller et al. [34] demonstrated the presence of wavelength regions with high polarization-dependent loss. An effect introduced by the cladding microstructure of hollow photonic fibers. This behavior was predicted by White et al. [35] for microstructured fibers. Here it is relevant to point out that the theoretical model we use assumes the fiber presents a negligible absorption. Besides, our measuring procedure uses output SOPs of linearly polarized signals with the same input azimuth angle but different wavelengths to confirm the fiber behaves as a homogeneous retarder. As a result of the previous information, it is necessary to verify that the wavelength regions used for the birefringence characterization present a uniform transmittance.

2.2 Experimental Setup

We divided the polarimetric setup into three sections. The first section produces a linearly polarized input signal whose azimuth angle can be modified by rotating a prism polarizer mounted on an automatically controlled rotation stage. In the second section, the probe signal couples to the photonic fiber input face and propagates along. The third section aims to send the signal emerging from the sample under evaluation to the detection system. Fig. 3 shows the complete experimental setup.

The experimental arrangement uses a tunable laser (TLS, Hewlett Packard 8168C) with a 1530 to 1560 nm operation band. Next to it, we have an isolator protecting the TLS diode from reflected light. The polarization controller (PC) is used to produce a circularly polarized beam. The coupling mount (C1) with a microscope objective (C0) generates a collimated light beam traveling through air to the prism polarizer (P). The incident circularly polarized beam is transformed by a calcite prism polarizer producing linearly polarized signals with specific azimuth angles. The prism polarizer is attached to a translation stage displacing it in and out the polarimetric setup and is mounted on a motorized mechanical support allowing the azimuthal angle variation. The polarized signal is launched to a coupling mount with a microscope objective (C2), also mounted on an automatic translation stage, allowing to remove and reposition this input port in the polarimetric setup. Light is launched into the microstructured fiber under test through coupler C2. The output light beam collimated by the aspheric collimator lens in the coupling mount (C3), travels by air to another coupling mount with a microscope objective (C4), connected to the polarization analyzer Agilent 8509C.

For each wavelength, it is necessary to create a reference frame for the polarization analyzer. For this purpose, the prism polarizer and the fiber sample (including couplers C2 and C3) can be removed from the polarimetric setup and repositioned using the platforms supporting them.

The experimental arrangement developed for evaluating the wavelength regions with low polarization-dependent loss (Fig. 4) is compatible with the polarimetric setup used to evaluate birefringence (Fig. 3). We changed the monochromatic light source (TLS) for a fiber broadband source with a 1510 to 1590 nm operation band (EDF light source) and the polarization analyzer for an optical spectral analyzer (OSA, Advantage, model Q8384). Using different orientations of the prism polarizer, we evaluated the changes introduced by the fiber sample, comparing the linearly polarized input spectra launched into the fiber with those measured at the fiber end.

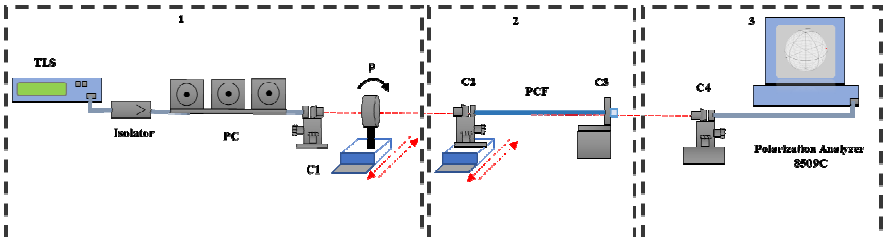

Fig. 3. Experimental setup used for: 1) the generation of the input linearly polarized signal, 2) the transmission of the signal through the fiber sample, and 3) the birefringence characterization through the evaluation of the state of polarization of the signal emerging from the photonic crystal fiber end face

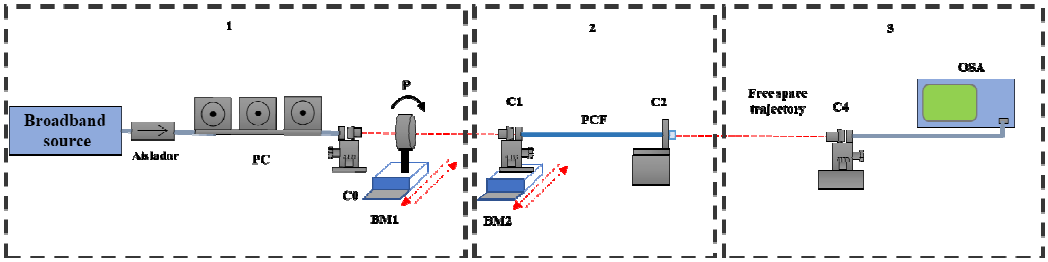

Fig. 4. Experimental setup used for the evaluation of the wavelength regions with polarization-dependent loss

2.3 Sample Preparation

Sample preparation consists of two main steps. In the first step, we subject the PCF sample tips to a heat treatment that allows us to collapse only the coating gaps in the end faces´ vicinity without causing damage to the cladding microstructure. We use conventional equipment to fuse fibers (ERICSON FSU-975) with a modified program to perform this task. In the second step, we carefully cleaned the fiber´s tip to remove impurities and moisture that may result from the handling process. Subsequently, a standard FC/UPC type connector for single-mode optical fibers is installed and fixed with epoxy type glue. After the epoxy solidification time has elapsed, we manually polished the PCF sample with optical grade sandpaper. The quality of end faces was verified using a microscope. Moreover, following the procedure suggested by the manufacturer in the datasheet, we used a 632 nm monochromatic beam to verify the far-field output beam distribution. We also confirmed the optical transmittance using a broadband source directly coupled to the sample.

3. RESULTS AND DISCUSSION

The samples used are commercial large-mode-area photonic glass fibers manufactured by the company NKT Photonics. The models selected were LMA-12 and LMA-25 with a hexagonal arrangement of holes in the cladding and a solid-core. The main characteristics of these fibers are shown in Table 1.

3.1 Wavelength Regions with Low Polarization-dependent Loss

At first, we evaluate the sample transmittance looking for a wavelength region where polarization-dependent loss is low and uniform. We used the experimental setup in Fig. 4, developed for input signals with linear states of polarization [20,36,37].

Table 1. Principals parameters of the fibers

Data	LMA 12	LMA 25
Core diameter	12.2 ± 0.5 µm	25 ± 1 µm
Modal diameter (MFD)	10.5 ± 1.0 µm for λ = 1550 nm	20.9 ± 2.0 for λ = 1064 nm
NA	0.09 ± 0.02 for λ = 1064 nm	0.05 ± 0.02 for λ = 1064 nm
Sample length	55 cm	93 cm

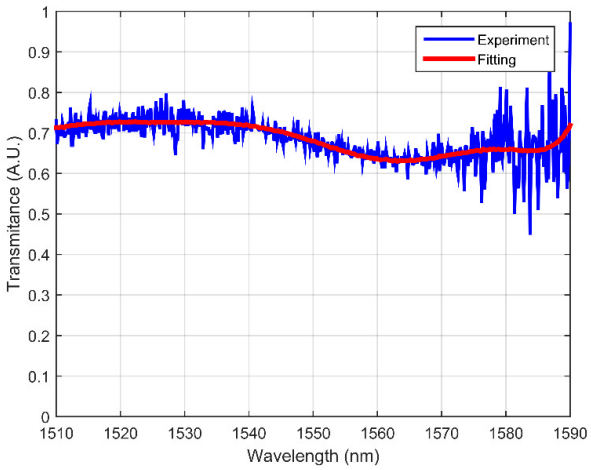

Fig. 5. Spectral transmittance for the PCF LMA-12 sample obtained for a linearly polarized SFS source (azimuth angle φ_{in} = 45 °)

The light source is a linearly polarized broadband source. 1) Initially, we capture the light spectra at the exit tip of the PCF sample associated with different azimuthal angles φ_{in} of the calcite polarizing prism. 2) Subsequently, we remove the PCF sample and capture the light spectra obtained from the calcite polarizing prism that correspond to the azimuth angles φ_{in} used for the polarizing prism. 3) Finally, we calculated the transmittance using the relation.

$$T(\varphi) = \frac{E_{out}(\varphi_{in})}{E_{in}(\varphi_{in})}, \quad (9)$$

where E_{out} is the output power spectrum and E_{in} is the input power spectrum associated with the same azimuthal angle of the polarizing prism φ_{in}.

The evaluation of the transmittance was carried out experimentally for 13 azimuth angles φ of the polarizing prism between 0 and 180 degrees in steps of 15 degree intervals. This sequence allows avoiding changes caused by the sample's alignment in the experimental setup when varying the angle φ_{in} of the calcite polarizing prism. It also helps faster measurements, lowering variations introduced by ambient temperature.

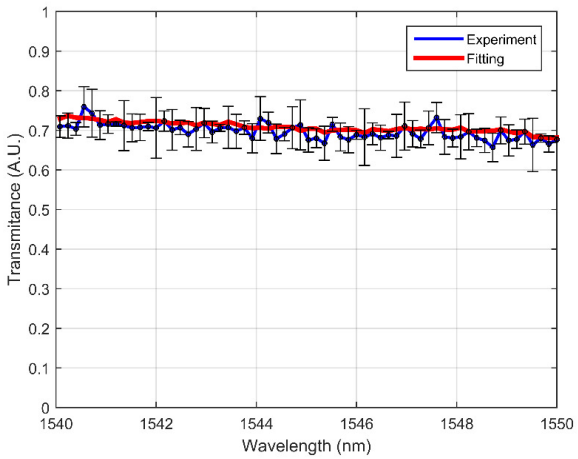

Fig. 6. Transmittance for the PCF LMA-12 sample for the spectral window between 1540 and 1550 nm for an azimuthal angle of the calcite polarizing prism φ_{in} = 45 °, experimental data (blue line) including standard deviation. The red line was obtained using a 10th-degree polynomial fitting of experimental data

We repeated the measurement ten times for each azimuth angle and calculated the experimental data´s standard deviation. The transmittance changes in Fig. 5 measured for φ_{in} = 45°, for the LMA-12 sample, show the PCF sample's sensitivity to polarized signals and external disturbances such as ambient laboratory temperature and vibrations. Considering stability, from this data, we selected the wavelength region from 1540 to 1550 nm to apply our polarimetric techniques (Fig. 6). We used a blue line for the experimental data. The red line corresponds to a 10th-degree polynomial fitting of data.

3.2 Identification of the Type of Retarder

Data shown in Fig. 6 indicate that even within the 1540 to 1550 nm wavelength band, ambient disturbances have an essential effect on the fiber transmittance. To minimize its contribution, we performed a fast evaluation of the input signal´s SOP evolution as the signal travels through the fiber. To obtain the wavelength scanning curves for different azimuth angles, we calibrated the polarization analyzer for 1545 nm (central wavelength). We scanned the signal wavelength using a fixed orientation for the prism polarizer (fixed azimuth angle of the input signal's linear polarization) this process takes approximately 6 minutes per wavelength. The output SOPs mapped on the Poincaré sphere are shown in Fig. 7 for LMA- 25 PCF. In this case, the azimuth angles of the input signal´s polarization varied from 0° to 180° with a step change of 10 degrees, and the wavelength scanning range presented in Fig. 7 varied from 1540 to 1550 nm (step 10 nm). For the LMA-25 sample, the output SOPs results shown in Fig. 8 correspond to a different wavelength scanning range (1549.1 to 1549.9 nm, step 0.1 nm), and we report three input azimuth angles (100°, 120°and 140°). Comparing these outcomes with the predictions shown in Figs. 1 and 2, we see that for both samples, the fiber birefringence is elliptical and presents a residual torsion.

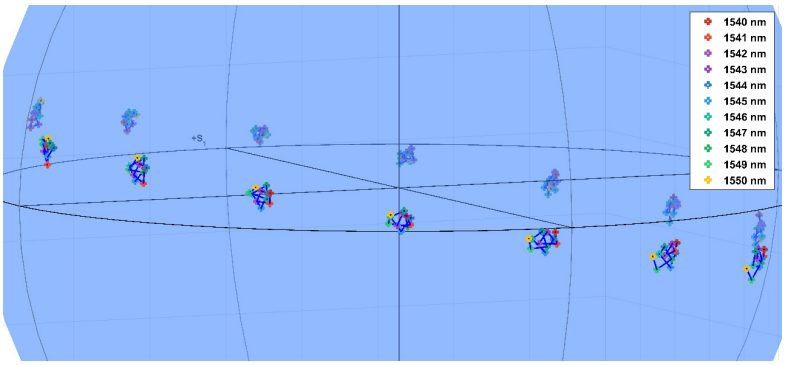

Fig. 7. SOP evolution of the signal through the LMA-12 sample, measured using wavelength scanning (1540 nm to 1550 nm, 10 nm step). The azimuth angles of the input signal´s polarization varied from 0° to 180° with a step change of 10 degrees.

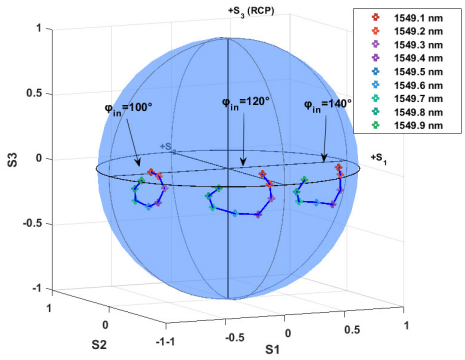

Fig. 8. SOP evolution of the signal through the LMA-25 sample, measured using wavelength scanning (1549.1 nm to 1549.9 nm, step 0.1 nm). The azimuth angles of the input linear polarization were 100°, 120° and 140°

3.3 Determination of Birefringence Parameters Using the Azimuth Scanning Technique

After verifying the fiber behaves as a homogeneous retarder with residual torsion, from the theoretical descriptions in [28,38], we learned the method in reference [20] could be applied to these samples. We launched a monochromatic linearly polarized signal at the fiber input and varied its azimuth angle from 0° to 180° (0.5° increment) [20]. Then, we registered the evolution of the output SOP. The first parameter obtained from these data is the azimuth angle (θ) of the fast birefringence axis. Using the first output SOP for which $S3_{out} = 0$ and its corresponding input SOP.

$$2\theta = 2\varphi_{in} + \frac{\varphi_{out} - 2\varphi_{in}}{2}, \quad (10)$$

where φ_{in} and φ_{out} are their azimuthal angles (Eq. 3).

Next, using the output SOP (S_{1out}, S_{2out}, S_{3out}) associated with the input polarization state for which $\varphi_{in} = \theta$ we can determine the ellipticity angle μ

$$\tan(2\mu) = \frac{1 - S_{1out}\cos(2\theta) - S_{2out}\sin(2\theta)}{S_{3out}}. \quad (11)$$

To calculate δ_E modulus-π, we go back to the output SOP for which S_{3out}=0,

$$\tan\left(\frac{\delta_E}{2}\right) = \frac{\tan[2(\varphi - \theta)]}{\sin(2\mu)} \quad (12)$$

The use of 0.5° increment between consecutive azimuth angles for the input SOPs allows a better precision in the determination of θ, μ and δ_E modulus-π. The experimental results obtained for the PCF samples sweeping the azimuth angle of a monochromatic signal with linear SOP are shown in Figs. 9 and 10 (blue lines). In these figures the red lines corresponds to the numerical simulation obtained using the values determined for the fast birefringence axis (θ), the ellipticity angle (μ), and the retardation angle (δ_E modulus- π).

The results shown in Figs. 9 and 10 demonstrate the appropriateness of the method used to determine the birefringence matrix parameters. The agreement between the experimental results and the numerical simulation is suitable for both PCFs. In particular, the graphical results show the homogeneous retarder model effectiveness in describing the PCF sample birefringence. We should mention that the simulations also match for the rest of the wavelengths (not shown) with the experimental results, as can be noticed in Table 2.

To discern the birefringence dispersion effects, we report the values determined for θ, μ y δ_E for different wavelengths. These data are presented in the graphs in Figs. 11 and 12, for PCF LMA-12, and PCF LMA-25, respectively, and in Table 2.

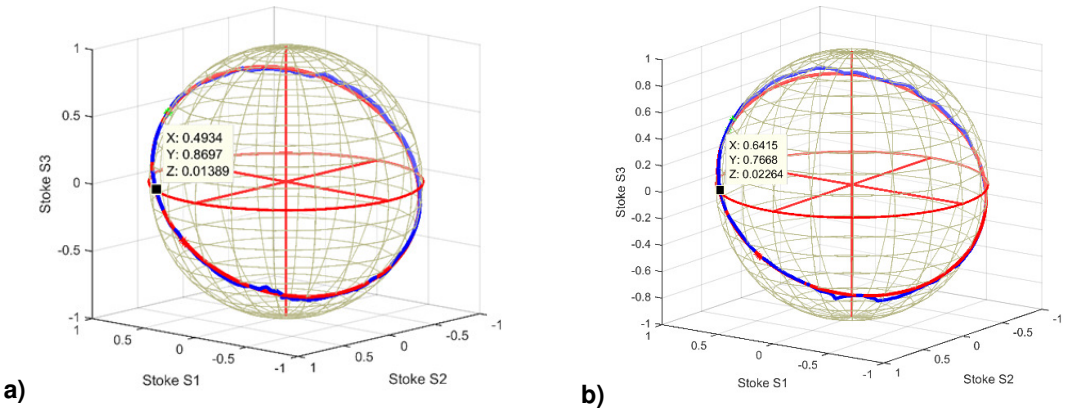

Fig. 9. Experimental results (blue curve) obtained for PCF LMA-12 sample applying azimuth sweeping to the linear SOP of the input monochromatic signal a) 1542 nm; b) 1543 nm. The red line corresponds to the numerical simulation using the values determined for θ, μ and δ_E modulus-π

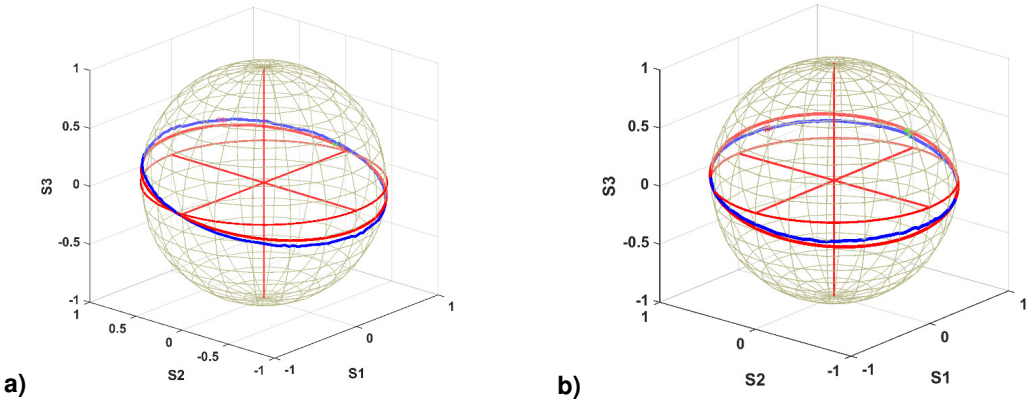

Fig. 10. Experimental results (blue curve) obtained for PCF LMA-25 sample applying azimuth sweeping to the linear SOP of the input monochromatic signal a) 154.4 nm; b) 1549.7 nm. The red line corresponds to the numerical simulation using the values determined for θ, μ and δ_E modulus-π

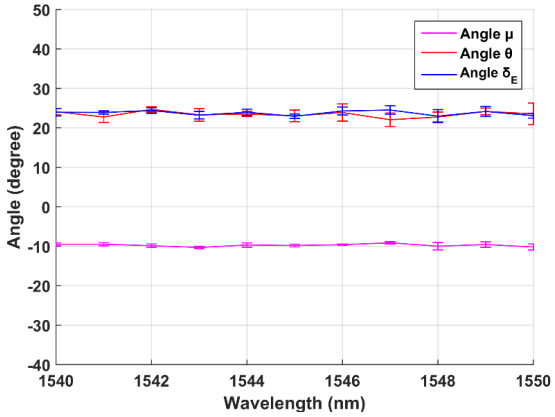

Fig. 11. Spectral dependence of the azimuth angle of the fast birefringence axis (θ), the ellipticity angle (μ) and the total retardation angle modulus-π (δ_E) for PCF LMA-12

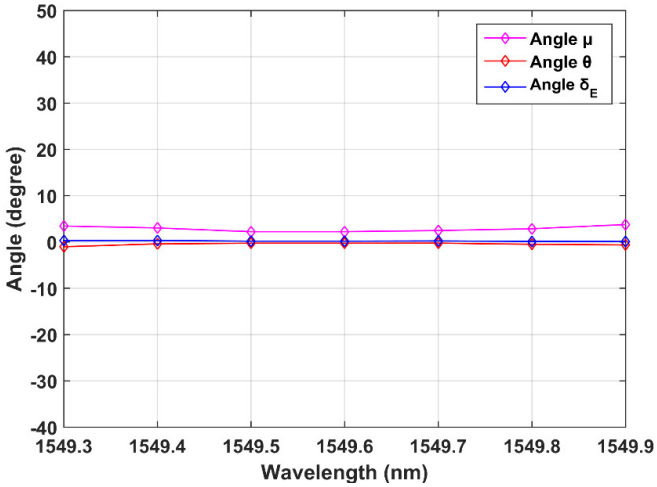

Fig. 12. Spectral dependence of the azimuth angle of the fast birefringence axis (θ), the ellipticity angle (μ) and the total retardation angle modulus-π (δ_E) for PCF LMA-25

Table 2. Birefringence parameters calculated for PCFs LMA-12 and LMA-25

LMA 12				LMA 25			
λ (nm)	θ (°)	μ (°)	δ_E (°)	λ (nm)	θ (°)	μ (°)	δ_E (°)
1540	24	-9	25	1549.3	-1	3	0
1541	23	-10	24	1549.4	-0	3	0
1542	24	-10	25	1549.5	-0	2	0
1543	25	-11	24	1549.6	-0	2	0
1544	23	-9	25	1549.7	-0	2	0
1545	24	-10	23	1549.8	-0	3	0
1546	24	-10	26	1549.9	-1	4	0
1547	23	-9	26				
1548	24	-9	24				
1549	24	-9	25				
1550	24	-11	22				

In Table 2 we rounded up the values calculated for the fast birefringence axis (θ), the ellipticity angle (μ), and the retardation angle (δ_E modulus-π).

Concerning the angles characterizing the polarization eigenmodes, we observe no significant change in the azimuthal angle θ (Figs. 11 and 12). The approximate value is 24° for PCF LMA-12 and 0° for PCF LMA-25. For the elliptic angle (μ), the higher variation was 2° for both samples. For LMA-25 it was equal to 3° and -9° for PCF LMA-12. As can be noted in Fig. 8, the behavior of sample LMA-25 is closer to that of a linear retarder than PCF LMA-12, even though the second one presents a stronger residual torsion.

The values of the delay angle δ_E modulus-π determined for PCF LMA-12 presented small fluctuations centered at 24° (Table 2) within the investigated wavelength range. Comparing the results shown in Fig. 7 with those reported in Fig. 5 in Ref. [39], we can conclude that the residual torsion of PCF LMA-12 is higher than 18 π rad/m. To determine the total retardation angle δ_E, it would be necessary, at first, to evaluate the residual torsion following the experiment reported in [39].

Regarding PCF LMA-25, the delay angle δ_E modulus-π presented minor fluctuations (Table 2). The result $\delta_E = 0$ would indicate that the polarization beatlength can be an integer multiple of ~93 cm in the absence of residual torsion. Nevertheless, comparing the curves in Fig. 8 with the experimental results in reference [39], we can notice that the average radius of the curves described for each azimuthal angle indicates that the residual torsion is low (~π rad/m). Therefore, the polarization beatlength of this PCF sample should be close to 93 cm [40]. This value is larger than that reported for conventional standard [41] and erbium doped fibers [37]. Additionally, the corresponding group birefringence in the vicinity of 1549 nm could be ~1.66×10^{-6} [12]. This value is two or three orders of magnitude lower than the values reported for PM or HiBi PCFs [10,12,42,43].

Both investigated fibers exhibit a low residual birefringence with a smooth spectral dependence in the wavelength window used for the evaluation.

4. CONCLUSION

The transmittance evaluation of both fibers from 1510 nm to 1590 nm showed the presence of a non-uniform wavelength behavior [35], enhanced by temperature-dependent changes. The wavelength-dependent variation in the fiber´s power contradicts the hypothesis that the power loss is negligible for short fiber lengths. Therefore, to satisfy this premise, it was necessary to select a suitable evaluation band. The band from 1540 nm to 1550 nm resulted appropriate for the application of wavelength-scanning, using a fast evaluation procedure to minimize temperature´s influence.

The wavelength-scanning results evidenced the presence of residual torsion, a feature avoiding the use of many of the measurement procedures developed for conventional non-intentionally birefringent fibers [40].

The matrix description of twisted fibers [28,38] indicates the method of reference [20] can be applied to these fibers. This procedure allows the determination of the parameters required to build

the fiber birefringence matrix. The agreement between the numerical simulations obtained for the azimuthal scanning and the experimental results was excellent, as expected.

For an evaluation performed between 1549.3 nm and 1549.8 nm, the ellipticity angle of PCF LMA-25 was ≤ 3°. Within this narrow band, this sample presented a nearly linear birefringence. For 1549 nm-1550 nm, the ellipticity angle of PCF LMA-12 was higher (9°-11°).

This work presents a measurement technique allowing the determination of the matrix birefringence of two types of large-mode-area photonic crystal fibers. This matrix operator is necessary to predict the evolution of the signal´s state of polarization as it travels along the PCF.

Further work is required to evaluate the fiber´s polarization beatlength when the fiber presents residual torsion.

DISCLAIMER

The products used for this research are commonly and predominantly use products in our area of research and country. There is absolutely no conflict of interest between the authors and producers of the products because we do not intend to use these products as an avenue for any litigation but for the advancement of knowledge. Funding by Conacyt and Centro De Investigación Científica Y De Educación Superior De Ensenada, Baja California.

COMPETING INTERESTS

Authors have declared that no competing interests exist.

REFERENCES

1. Zhaoming Zhu, Thomas G Brown. Stress-induced birefringence in microstructured optical fibers. Opt. Lett. 2003;28:2306-2308.
2. Wegmuller M, Legre M, Gisin N, Ritari T, Ludvigsen H, Folkenberg JR, Hansen KP. Experimental investigation of wavelength and temperature dependence of phase and group birefringence in photonic crystal fibers. Proceedings of 2004 6th International Conference on Transparent Optical Networks (IEEE Cat. No.04EX804). 2004;2:111-114.
DOI: 10.1109/ICTON.2004.1361980
3. Tarnowski K, Martynkien T, Mergo P, et al. Compact all-fiber source of coherent linearly polarized octave-spanning supercontinuum based on normal dispersion silica fiber. Scientific Report. 2019;9:12313.
Available:https://doi.org/10.1038/s41598-019-48726-9
4. Davtyan S, Novoa D, Chen Y, Frosz MH, P St J Russell. Polarization-tailored raman frequency conversion in chiral gas-filled hollow-core photonic crystal fibers. Phys. Rev. Lett. 2019;122(14):143902.
5. Edavalath NN, Günendi MC, Beravat R, Wong GKL, Frosz MH, Ménard JM, P St J Russell. Higher-order mode suppression in twisted single-ring hollow-core photonic crystal fibers. Opt. Lett. 2017;42:2074-2077.
6. Roth P, Chen Y, Günendi MC, Beravat R, Edavalath NN, Frosz MH, et al. Strong circular dichroism for the HE11 mode in twisted single-ring hollow-core photonic crystal fiber. OPTICA. 2018; 5(10):1315-1321.
DOI: 10.1364/OPTICA.5.001315
7. Cassataro M, Novoa D, Guenendi MC, Edavalath NN, Frosz MH, Travers JC, et al. Generation of broadband mid-IR and UV light in gas-filled single-ring hollow-core PCF. Optics Express. 2017;25(7): 7637-7644.
DOI: 10.1364/OE.25.007637
8. Shou-Fei Gao, Ying-Ying Wang, Wei Ding, and Pu Wang. Hollow-core negative-curvature fiber for UV guidance. Opt. Lett. 2018;43:1347-1350.
9. Saitoh K, Koshiba M. Single-polarization single-mode photonic crystal fibers. in IEEE Photonics Technology Letters. 2003;15(10):1384-1386.
DOI: 10.1109/LPT.2003.818215
10. Ortigosa-Blanch A, Knight JC, Wadsworth WJ, Arriaga J, Mangan BJ, Birks TA, P St J Russell. Highly birefringent photonic crystal fibers. Opt. Lett. 2000;25(18):1325-1327.
11. Schreiber T, Schultz H, Schmidt O, Röser F, Limpert J, Tünnermann A. Stress-induced birefringence in large-mode-area micro-structured optical fibers. Opt. Express. 2005;13:3637-3646.
12. Peyrilloux A, Chartier T, Hideur A, Berthelot L, Mélin G, Lempereur S, Pagnoux D, Roy P. Theoretical and experimental study of the birefringence of

a photonic crystal fiber. J. Lightwave Technol. 2003;(21):536.
13. Antkowiak M, Kotynski R, Nasilowski T, Lesiak P, Wojcik J, Urbanczyk W, Berghmans F, Thienpont H. Phase and group modal birefringence of triple-defect photonic crystal fibres. Journal of Optics A: Pure and Applied Optics. 2005;7(12):763–766.
14. Ming-Yang Chen. Polarization-maintaining large-mode-area photonic crystal fibres with solid microstructured cores. J. Opt. A: Pure Appl. 2007;(9):868.
15. Wang X, Dong X, Xie Z. Measurement and analysis of the birefringence of photonic crystal fiber with wavelength scanning method. Opt Quant Electron. 2007;(39):1081.
Avilable:https://doi.org/10.1007/s11082-007-9166-5
16. Buczynski R, Kujawa I, Pysz D, Martynkien T, Berghmans F, Thienpont H, Stepien R. Highly birefringent soft glass rectangular photonic crystal fibers with elliptical holes. Appl Phys. 2010;(B 99):13–17.
17. Folkenberg JR, Nielsen MD, Mortensen NA, Jakobsen C, Simonsen HR. Polarization maintaining large mode area photonic crystal fiber. Opt. Express. 2004;12:956-960.
18. Ritari T, Ludvigsen H, Wegmuller M, Legré M, Gisin N, Folkenberg JR, Nielsen MD. Experimental study of polarization properties of highly birefringent photonic crystal fibers. Opt. Express. 2004;(12):5931-5939.
19. Xu S, Shao H, Li C, Xing F, Wang Y, Li W. Linear birefringence measurement method for an optical fiber current sensor. Sensors. 2017;17(7):1556.
DOI:10.3390/s17071556A
20. Rojas-Sanchez A, Tentori D. Simple method for the characterization of birefringence of single-mode optical fibers. OSA Continuum 3. 2020;1650-1656.
21. Ibarra-Escamilla B, Kuzin EA, Gutierrez-Zainos F, Tellez-Garcia R, Haus JW, Rojas-Laguna R, Estudillo-Ayala JM. Measurement of beat length in short low-birefringence fibers using the fiber optical loop mirror. Optics Communications. 2003;217(1-6):211-219.
22. Ramaswamy V, Standley RD, Sze D, French WG. Polarization effects in short length, single mode fiber. Bell Sys. Tech. J. 1978;57(3):635-651.
23. Takada K, Noda J, Ulrich R. Precision measurement of modal birefringence of highly birefringent fibers by periodic lateral force. Appl. Opt. 1985;24:4387-4391.
24. Barlow A. Optical-fiber birefringence measurement using a photo-elastic modulator. in Journal of Lightwave Technology. 1985;3(1):135-145.
25. Chang-Seok Kim, Young-Geun Han, Sova RM, Un-Chul Paek, Youngjoo Chung, Kang JU. Optical fiber modal birefringence measurement based on Lyot-Sagnac interferometer. in IEEE Photonics Technology Letters. 2003;15(2):269-271.
26. Calvani R, Caponi R, Cisternino F. Polarization measurements on single-mode fibers. in Journal of Lightwave Technology. 1989;7(8):1187-1196.
27. Hauge PS, Muller RH, Smith CG. Conventions and formulas for using the Mueller-Stokes calculus in ellipsometry. Surf. Sci. 1980;96(1-3):81–107.
28. Tentori D, Garcia-Weidner A, Ayala-Díaz C. Birefringence matrix for a twisted single-mode fiber: Photoelastic and geometrical contributions. Optical Fiber Technology. 2012;18:14–20.
29. Tentori D, Garcia-Weidner A. Jones birefringence in twisted single-mode optical fibers. Opt. Express. 2013;21:31725-31739.
30. Russell P. Photonic crystal fibers. Science. 2003;(299(5605)):358-362.
31. Chong JH, Rao MK, Zhu Y, Shum P. An effective splicing method on photonic crystal fiber using CO 2 laser. IEEE Photonics Technology Letters. 2003;5(7):942-944.
DOI: 10.1109/LPT.2003.813410
32. Xiao L, Jin W, Demokan MS. Fusion splicing small-core photonic crystal fibers and single-mode fibers by repeated arc discharges. Optics letters. 2007;(32(2)):115-117.
DOI: https://doi.org/10.1364/OL.32.000115
33. Xiao L, Demokan MS, Jin W, Wang Y, Zhao CL. Fusion splicing photonic crystal fibers and conventional single-mode fibers: Microhole collapse effect. Journal of lightwave technology. 2007;(25(11)):3563-3574.
34. Mark Wegmuller, Matthieu Legré, Nicolas Gisin, Theis P Hansen, Christian Jakobsen, Jes Broeng. Experimental investigation of the polarization properties of a hollow core photonic bandgap fiber for

1550 nm. Opt. Express. 2005;13:1457-1467.
35. White TP, McPhedran RC, de Sterke CM, Botten LC, Steel MJ. Confinement losses in microstructured optical fibers. Opt. Lett. 2001;26:1660-1662.
36. Tentori D, Ayala-Díaz C, Treviño-Martínez F, Mendieta-Jiménez FJ. Evaluation of the residual birefringence of single-mode erbium-doped silica fibers. Opt. Commun. 2007;(271(1)):73-80.
37. Treviño-Martínez F, Tentori D, Ayala- Díaz C, Mendieta-Jiménez FJ. Birefringence assessment of single-mode optical fibers. Opt. Express 2005;13:2556-2563.
38. Tentori D, García-Weidner A. Right- and left-handed twist in optical fibers. Rev. Mex. Fis. 2014;60:69-74.
39. Tentori D, Ayala Díaz C. Twist induced birefringence in fibers and optical rotation. Proc. SPIE. 2009;7499-10.
40. Tentori D, Garcia-Weidner A, Kuzin E. On the birefringence evaluation of single-mode fibers. Rev. Mex. Fıs. 2016;(62):381-392.
41. He Wen, Matthew A. Terrel Hyang Kyun Kim, Michel JF. Digonnet, Shanhui Fan. Measurements of the birefringence and verdet constant in an air-core fiber. J. Lightwave Technol. 2009;(27):3194-3201.
42. Kazunori Suzuki, Hirokazu Kubota, Satoki Kawanishi, Masatoshi Tanaka, Moriyuki Fujita. Optical properties of a low-loss polarization-maintaining photonic crystal fiber. Opt. Express. 2001;9:676-680.
43. Ortigosa-Blanch A, Knight JC, Wadsworth WJ, Arriaga J, Mangan BJ, Birks TA, P St J Russell. Highly birefringent photonic crystal fibers. Opt. Lett. 2000;25:1325-1327.

Peer-review history:
The peer review history for this paper can be accessed here:
http://www.sdiarticle4.com/review-history/67243